

## Electronic Supplementary Information for

# Coalescence and shape oscillations of Au nanoparticles in CO<sub>2</sub> hydrogenation for methanol reaction

### Reconstruction of (200) plane of the Au NPs

In fact, the thermodynamic principles of the Au NPs (111) surface and (200) reconstruction are essentially identical, and they are both the process of surface energy becoming stable. We know from Fig. 4 that the reconstruction process of Au NPs (200) surface is:  $(200) \rightleftharpoons *(hkl)$ . DFT calculation results show that with the increase of gas molecular coverage, the adsorption of CO and H<sub>2</sub>O will reduce the surface energy of Au NPs (200) surface and (311), (331) high index surface to varying degrees (Fig.5c,d and Tables S-3-S-4). The high index surface adsorbed with the product gas obviously has lower surface energy.

For example, when the CO molecular coverage is 1 ML, the surface energy of (200) surface is 0.653 eV, while the surface energy of high index (311) and (331) surface are 0.261 and 0.362 eV respectively. When the H<sub>2</sub>O molecular coverage is 1 ML, the surface energy of (200) surface is 0.535 eV, while the surface energy of high index (311) surface and (331) surface are 0.353 and 0.275 eV respectively. Especially, when H<sub>2</sub>O has high cover ( $\theta = 2$  ML) high index (311) and (331) faces even produce negative surface energy (-0.33 eV, -0.033 eV). Therefore, when CO and / or H<sub>2</sub>O are adsorbed, the Au NPs (200) surface will change to a more stable high index surface. After gas desorption, the high index surface recovers the original surface energy. At this time, the (200) surface is more stable than the high index surface, so the reconstruction of the high index surface (200) surface will occur.

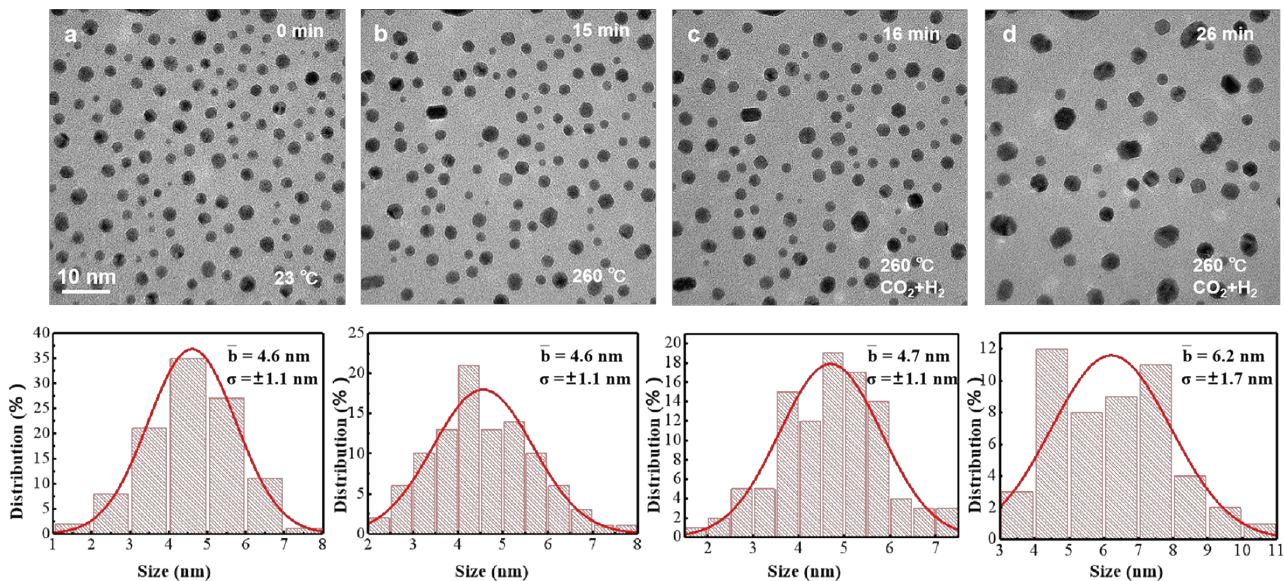


**Figure S-1.** The change process of Au NPs during CO<sub>2</sub> hydrogenation. The statistical size distribution of the Au NPs are located below the TEM picture. (a) Image of the morphology and size of Au NPs at room temperature, where the size distribution shows the average particle size of 4.6 nm, variance of 1.1nm. (b) Image of morphology and size of Au NPs after heat preservation 15 min at 260°C, when the size distribution shows the average particle size of 4.6 nm, variance of 1.1nm. (c) Changes in the morphology and size of the Au NPs after introduction into the reaction gas at 260°C. The particles size distribution shows the average particle size of 4.7 nm, variance of 1.1nm. (d) The morphology and size of the Au NPs changed significantly after 10 min of the catalytic reaction, with the average particle size of 6.2 nm, variance of 1.7 nm.

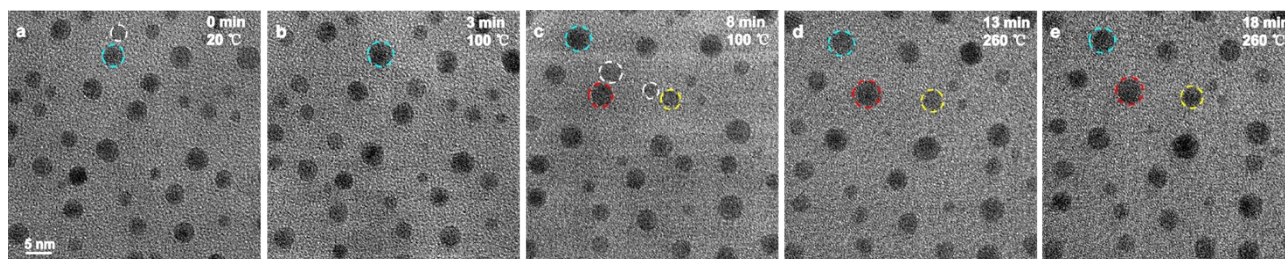


**Figure S-2.** Time resolved TEM images showing the results of the in situ heating of Au NPs. In the experiment, the effect of the reaction gas was not investigated, and only that of the temperature and electron beam was assessed. (a) Original distribution of the Au NPs at room temperature. (b) In situ heating to 100 °C, in which only two Au NPs with diameters of 2.2 and 3 nm are observed to coalesce, while the other particles remained stable. After 5 min of heating at 100 °C, the Au NP system in Fig. (c) remained stable without coalescence. (d) Distribution of the Au NPs with further in situ heating to 260 °C. Some small Au NPs coalesced, while the Au NPs sized  $\geq 5$  nm remained stable. (e) After 5 min of in situ heating at 260 °C, the Au NPs did not coalesce.

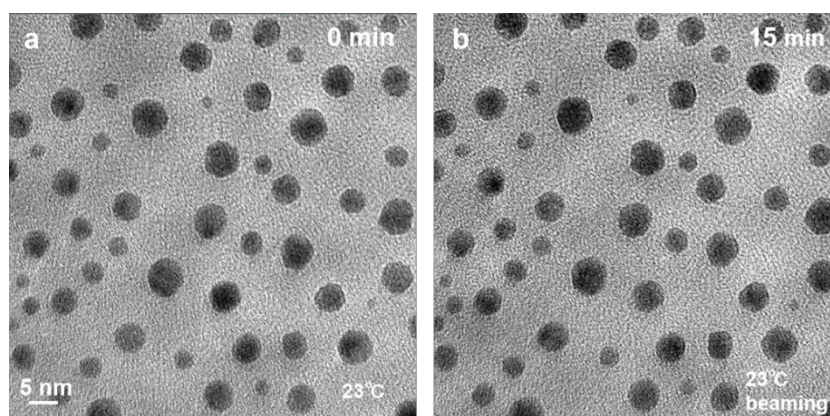


**Figure S-3.** Comparison before and after continuous irradiation of the Au NPs. (a) Observe the distribution of the Au NPs at room temperature in a selected region. At 23°C, the acceleration voltage was 200 kV (the electron incident energy was  $\sim 172$  keV) and the electron beam dose required for adjusting the experiment was  $1550 \text{ e}^-/\text{Å}^2/\text{s} \approx 2.5 \text{ Å}^2/\text{cm}^2$ . (b) The TEM images of the Au NPs obtained after 15 min of continuous irradiation of the same region, the coalescence of the Au

NPs didn't occur. Therefore, it can be directly demonstrated that the electron beam dose action is negligible in the experiments.

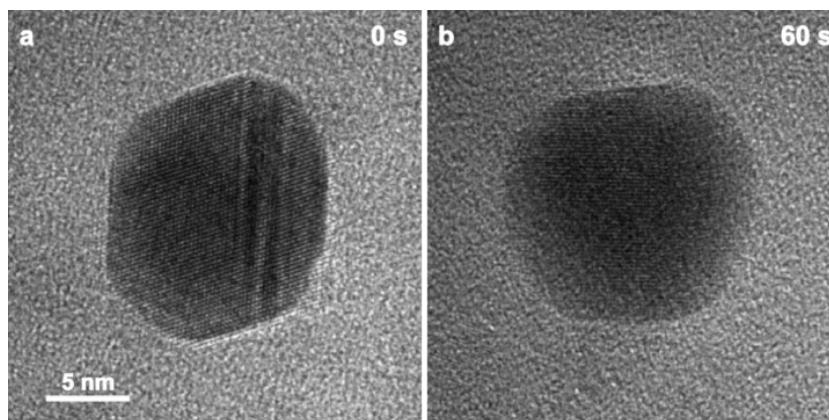


**Figure S-4.** Time-resolved TEM images of the reshaping of an Au NP under atmospheric pressure of  $\text{CO}_2+\text{H}_2$  (1:3) at 260 °C. (a) Polygynous Au NP at 0 s. (b) After turning off the electron beam for 60 s, the shape of the Au NP changed.

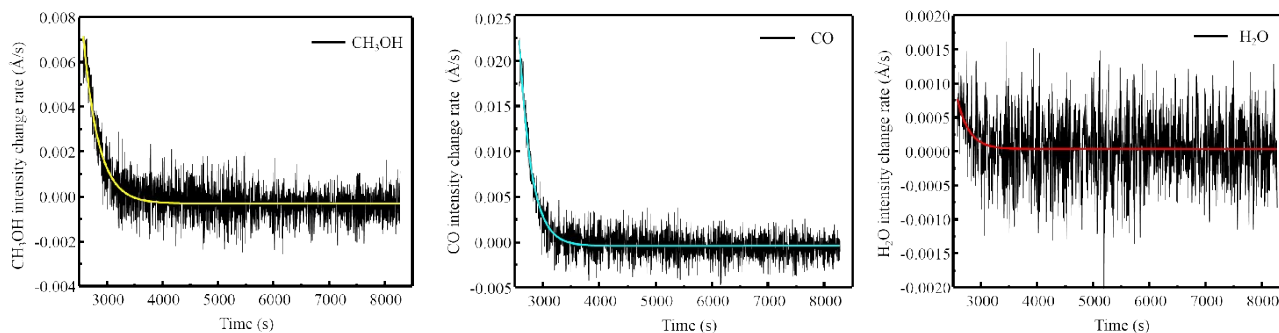


**Figure S-5.**  $\text{CO}_2$  hydrogenation reduction results of the Au NPs detected by a mass spectrometer connected to the exhaust of the in situ TEM holder at 260 °C when the electron beam was turned off. The smooth colored lines serve as guides. The result shows the change rate of the reaction product gas intensity as a function of time. The existence of  $\text{CH}_3\text{OH}$ ,  $\text{CO}$ , and  $\text{H}_2\text{O}$  in the  $\text{CO}_2$  hydrogenation reduction reaction system is confirmed. Note that our experiment used a micro-reactor, which has an extremely low reaction gas content. The mass spectrometric data only illustrates the types of gas generated and cannot be used as an evaluation for the catalytic performance of the Au NPs.

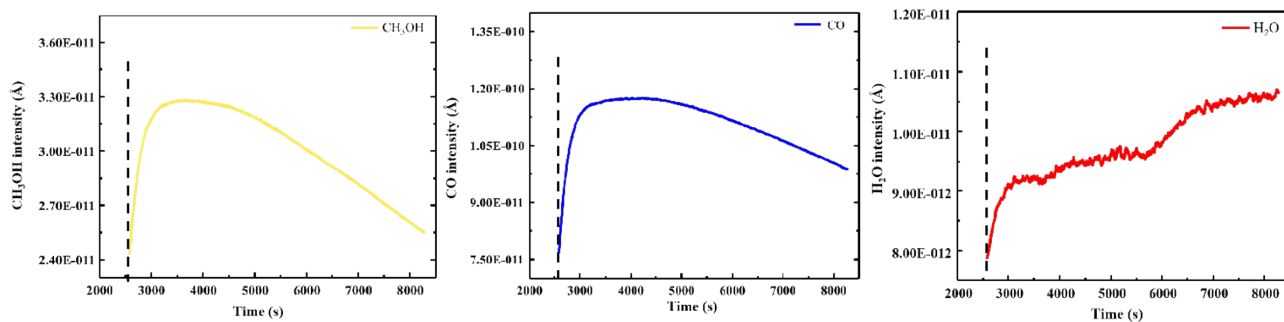


**Figure S-6.** The online mass spectrometer results show the change curve of product gas intensity with reaction time. The black line segments indicate the time of passing into the reaction gas. The gas strength of the CH<sub>3</sub>OH, CO, and H<sub>2</sub>O increases after passing into the reaction gas. And over the time range of our in situ observations (2000-4000s) the product gas strength continuously increases to a stable presence. Therefore, the product gas data provided by online mass spectrometer can demonstrate that our study is carried out under the desired catalytic activity.

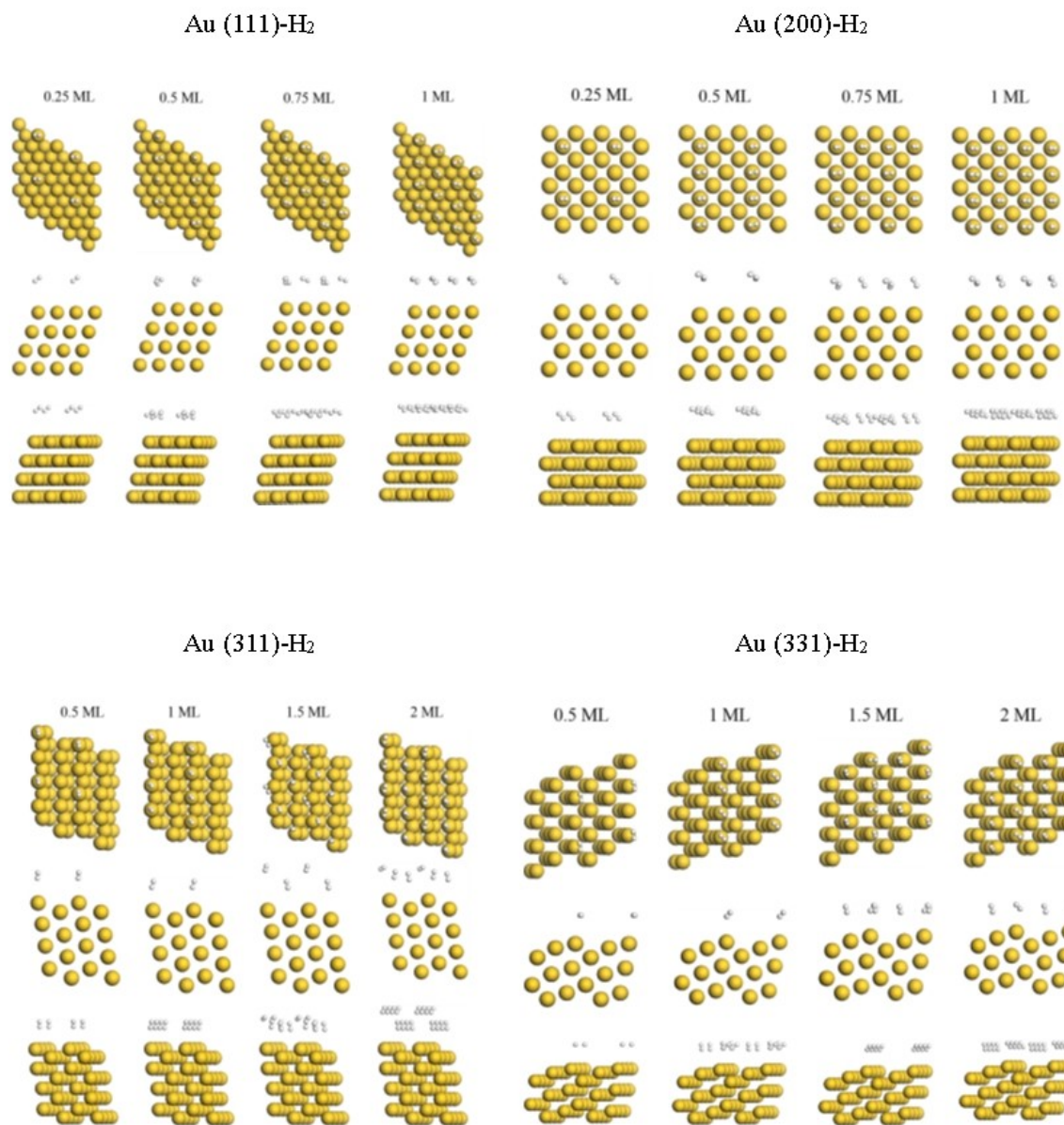


**Figure S-7.** Models of various Miller indices of the Au slabs at different H<sub>2</sub> coverages identified by the DFT calculations.

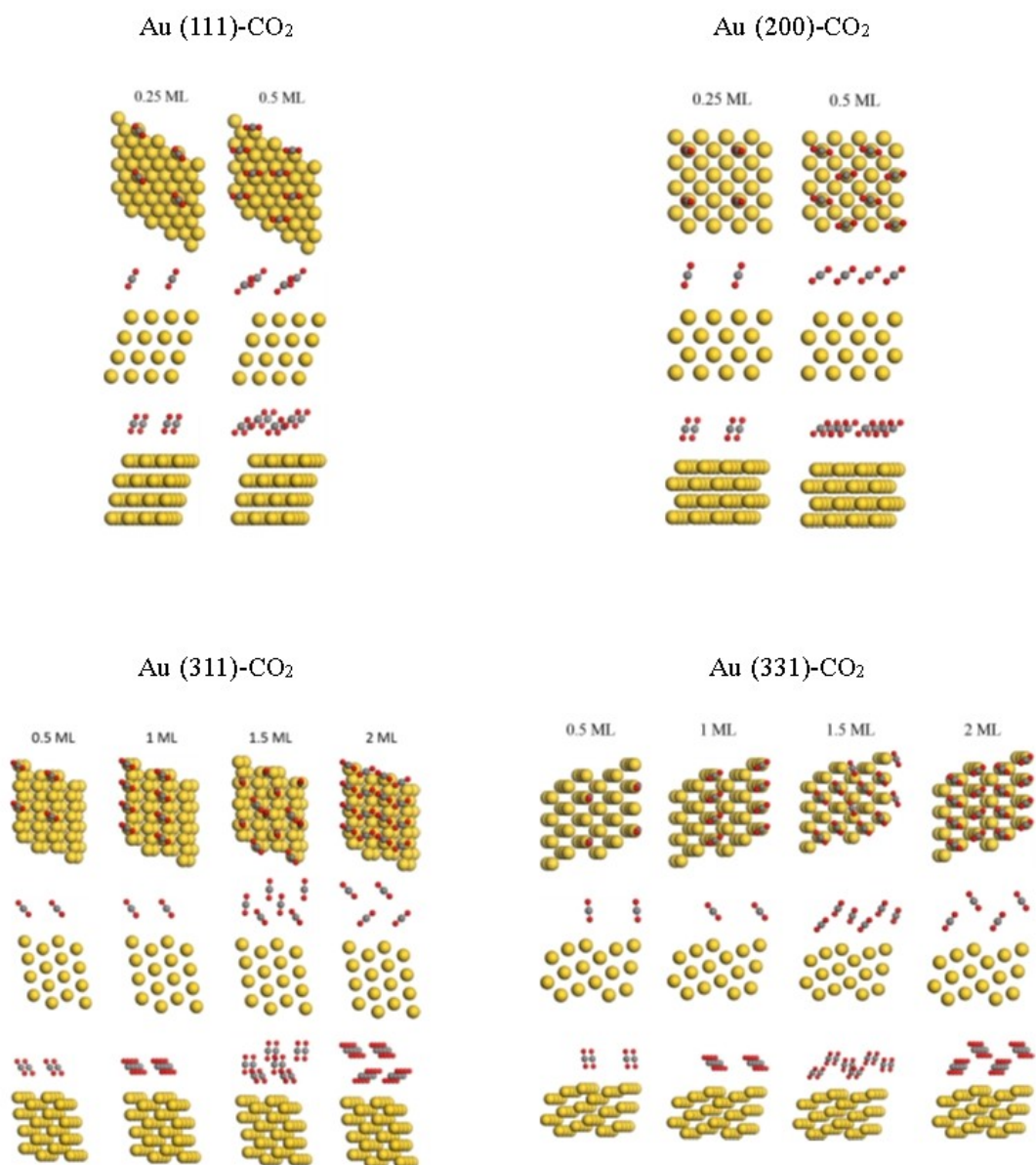


**Figure S-8.** Models of various Miller indices of the Au slabs at different CO<sub>2</sub> coverages identified from the DFT calculations.

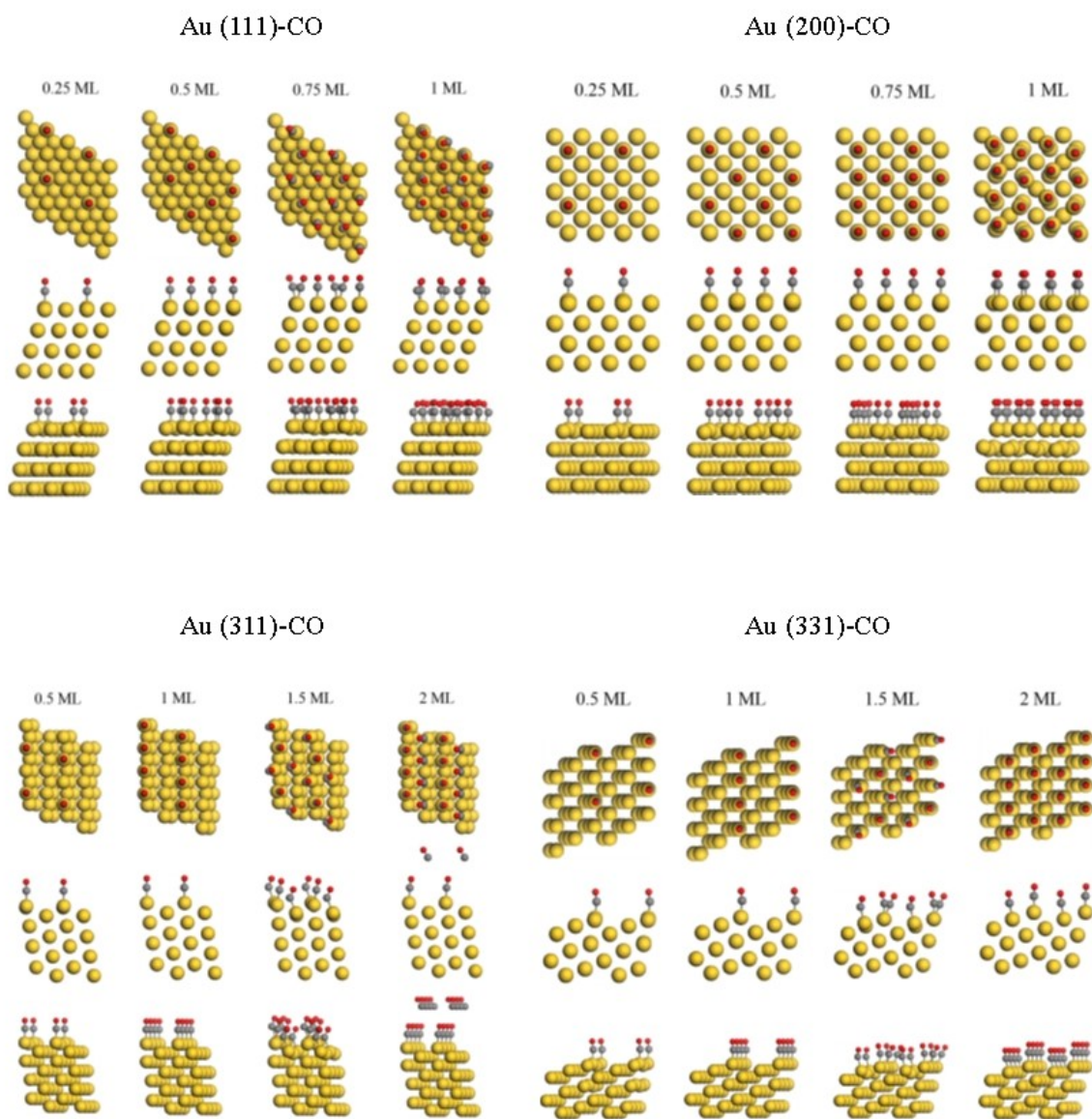


**Figure S-9.** Models of various Miller indices of the Au slabs at the different CO coverages identified from the DFT calculations.

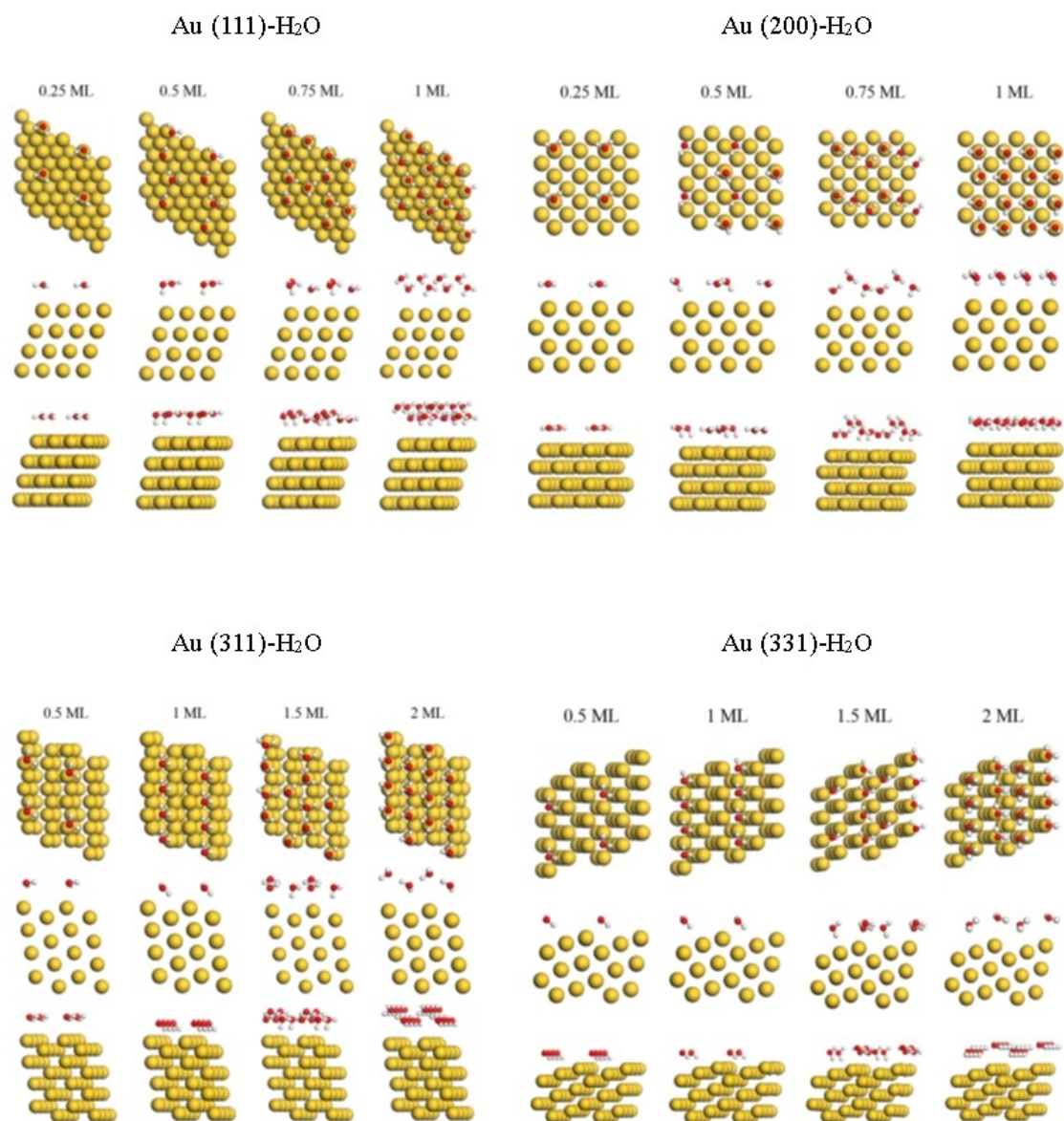


**Figure S-10.** Models of various Miller indices of Au slabs at different H<sub>2</sub>O coverages identified from the DFT calculations .

**Table S-1.** Calculated adsorption energies (eV) of the gas molecules with different coverages on the investigated Au (111) facets.

Gas Molecules	Coverage (ML)				
	0	0.25	0.5	0.75	1
H <sub>2</sub>	0.626	0.625	0.625	0.626	0.630
CO <sub>2</sub>	0.626	0.619	0.614		
CO	0.626	0.599	0.609	0.635	0.706
H <sub>2</sub> O	0.626	0.610	0.533	0.465	0.355

**Table S-2.** Calculated adsorption energies (eV) of the gas molecules with different coverages on the investigated Au (200) facets.

Gas Molecules	Coverage (ML)				
	0	0.25	0.5	0.75	1
H <sub>2</sub>	0.733	0.732	0.733	0.732	0.734
CO <sub>2</sub>	0.733	0.733	0.719	-	-
CO	0.733	0.685	0.647	0.662	0.653
H <sub>2</sub> O	0.733	0.718	0.654	0.585	0.535

**Table S-3.** Calculated adsorption energies (eV) of the gas molecules with different coverages on the investigated Au (311) facets.

Gas Molecules	Coverage (ML)				
	0	0.5	1	1.5	2
H <sub>2</sub>	0.764	0.762	0.768	0.758	0.769
CO <sub>2</sub>	0.764	0.771	0.952	0.763	1.099
CO	0.764	0.6	0.261	0.629	0.382
H <sub>2</sub> O	0.764	0.714	0.353	0.345	-0.33

**Table S-4.** Calculated adsorption energies (eV) of the gas molecules with different coverages on the investigated Au (331) facets.

Gas Molecules	Coverage (ML)				
	0	0.5	1	1.5	2
H <sub>2</sub>	0.718	0.712	0.636	0.709	0.637
CO <sub>2</sub>	0.718	0.532	0.787	0.705	0.898
CO	0.718	0.603	0.362	0.528	0.397
H <sub>2</sub> O	0.718	0.659	0.275	0.438	-0.033